

Electrochemical Impedance Spectroscopy of Core-Shell Nanofiber Cathodes, with $\text{Ce}_{0.9}\text{Gd}_{0.1}\text{O}_{1.95}$ (Core) and Cu-Doped $\text{La}_{0.6}\text{Sr}_{0.4}\text{MnO}_3$ (Shell), for Application in Solid Oxide Fuel Cells

Caterina Sanna,^[a] Paola Costamagna,^{*[a]} and Peter Holtappels^[b, c]

Several core-shell nanofiber electrodes are prepared through electrospinning and tested for application as intermediate-temperature solid oxide fuel cell (IT-SOFC) cathodes. The materials investigated are $\text{La}_{0.6}\text{Sr}_{0.4}\text{MnO}_3$ (LSM), $\text{La}_{0.6}\text{Sr}_{0.4}\text{Cu}_{0.1}\text{Mn}_{0.9}\text{O}_{3-\delta}$ (LSCuM_1), and $\text{La}_{0.6}\text{Sr}_{0.4}\text{Cu}_{0.2}\text{Mn}_{0.8}\text{O}_{3-\delta}$ (LSCuM_2) perovskites, used at the shell side of the nanofibers. $\text{Ce}_{0.9}\text{Gd}_{0.1}\text{O}_{1.95}$ (GDC10) fluorite is used as the core material. The electrochemical characterization of the core-shell nanofiber electrodes is performed through electrochemical impedance

spectroscopy (EIS). The EIS results are reported and discussed based on equivalent circuit modeling. The polarization resistance of the GDC10/LSM core-shell nanofibers electrodes is $R_p \sim 4.5 \Omega \text{cm}^2$ at 650°C . Improvement is accomplished with GDC10/LSCuM_1 and GDC10/LSCuM_2 core-shell nanofibers, with $R_p \sim 1.8 \Omega \text{cm}^2$ and $1.7 \Omega \text{cm}^2$ respectively at 650°C . Post-test SEM characterization is carried out, to ascertain possible degradation and identify the most promising shell perovskite.

Introduction

Perovskites are versatile metal oxides that have gained wide attention as cathode materials for intermediate-temperature solid oxide fuel cells (IT-SOFCs). The perovskite crystal structure, described with the general formula ABO_3 , can be modified by substituting atoms in the A and B sites, triggering electronic and/or oxygen ion conductivity and electrocatalytic activity.^[1–4] Among all perovskites, strontium-substituted lanthanum manganite ($\text{La}_{1-x}\text{Sr}_x\text{MnO}_3$, LSM) is considered the state-of-the-art cathode for high-temperature solid oxide fuel cells (HT-SOFCs). In the LSM perovskite, the La^{3+} ion placed in the A-site is substituted with an Sr^{2+} ion, leading to the formation of an electric hole, with consequent oxidation of an Mn atom, from Mn^{3+} to Mn^{4+} .^[2,3] Indeed, the Sr-doping significantly increases

the electrical conductivity of LaMnO_3 , which is 83 Scm^{-1} at 800°C , reaching 320 Scm^{-1} at 800°C with the $\text{La}_{0.6}\text{Sr}_{0.4}\text{MnO}_3$.^[2] Nonetheless, the current trend toward decreasing operating temperature makes it necessary to study more complex electrode architectures and materials, suitable for intermediate-temperature applications. Regarding advanced electrode architectures, electrospinning is an innovative technique to obtain three-dimensional nanofiber electrodes which have been demonstrated to provide promising performance.^[5] Electrospinning is based on the application of a high voltage between the metal needle of a syringe containing the metal precursor solution and the collector where the nanofibers are deposited. The electrospinning process is regulated by several parameters that need careful setting for each case study. In particular, the solution flow rate, the applied voltage, and the relative humidity affect the morphology of the nanofibers. Once a satisfactory set of operational parameters has been identified, electrospinning ensures high reproducibility of the results. Nanofiber-based electrodes have several advantages over the common powder-based electrode, such as high void degree and high active surface. Even more important, nanofibers ensure a continuous path for both electrons and oxygen ions, overcoming the bottleneck problem occurring in powder-based electrodes.^[6] For these reasons, nanofiber-based electrodes have demonstrated better results compared to powder-based ones, which are state-of-the-art.^[3,7–9] Among all the nanofiber geometries, that of core-shell appears particularly interesting. Core-shell electrospinning can be achieved using a syringe with two coaxial needles, enabling the simultaneous ejection of two different solutions, which results in composite nanofibers with a core material different from the shell. Composite electrodes have already been widely used in powder-based electrodes, where the electronic conductor perovskite (i.e., LSM) has been mixed with an ionic conductor material. Ytria stabilized zirconia,

[a] Dr. C. Sanna, Prof. P. Costamagna
 DCCI, Department of Chemistry and Industrial Chemistry
 University of Genoa
 Via Dodecaneso 31, I-16146 Genoa (Italy)
 E-mail: paola.costamagna@unige.it
 Homepage: <https://rubrica.unige.it/personale/VUZCXVlu>

[b] Dr. P. Holtappels
 DTU Energy, Department of Energy Conversion and Storage
 Technical University of Denmark
 Elektrovej 375, DK-2800 Kgs. Lyngby (Denmark)

[c] Dr. P. Holtappels
 Present address:
 Karlsruhe Institute of Technology (KIT)
 Institute for Micro Process Engineering (IMVT)
 Hermann-von-Helmholtz-Platz 1, 76344 Eggenstein-Leopoldshafen (Germany)

Supporting information for this article is available on the WWW under <https://doi.org/10.1002/celec.202300101>

© 2023 The Authors. ChemElectroChem published by Wiley-VCH GmbH. This is an open access article under the terms of the Creative Commons Attribution License, which permits use, distribution and reproduction in any medium, provided the original work is properly cited.

((ZrO₂)_{1-x}(Y₂O₃)_x, YSZ) and gadolinium doped ceria (Ce_{1-x}Gd_xO_{1-δ}, GDC), which represent the state-of-the-art electrolytes respectively for high and intermediate temperature application, have been widely used for the preparation of LSM-based composite electrodes, achieving interesting results.^[10–14] Composite electrodes have been demonstrated to improve electrochemical performance by extending the triple-phase-boundary (TPB) into the electrode thickness.^[15–17] This extension requires percolation of both the electronic and the ionic conducting particles, which needs careful design of the electrode composition, based on the dimensions of the starting powder particle dimensions.^[17,18] During functioning, if agglomeration or other morphological modifications take place, percolation can be lost, with a dramatic loss of performance.^[16] Core-shell nanofiber electrodes reproduce the same principle as composite electrodes, with the advantage that percolation is spontaneously ensured by the nanofibers themselves. In this respect, to the best of the authors' knowledge, one previous study was proposed, investigating core-shell nanofiber cathodes coupling YSZ and LSM, for HT-SOFC applications in the temperature range 850 °C–1150 °C.^[19] It was demonstrated that better performance was achieved when the ionic conductor (YSZ) was the core and the electronic conductor (LSM) was the shell of the nanofibers. Nevertheless, at present, there is a gap in the literature regarding the development of core-shell nanofibers specifically devoted to IT-SOFCs, employing GDC as the oxygen ion conductor.

Besides the development of advanced electrode architectures, innovative electrocatalytic materials are under development for IT-SOFCs, often based on mixed ionic and electronic conductors (MIECs). Lanthanum strontium cobalt ferrite (La_{1-x}Sr_xCo_{1-y}Fe_yO_{3-δ}, LSCF) and barium strontium cobalt ferrite (Ba_{1-x}Sr_xCo_{1-y}Fe_yO_{3-δ}, BSCF) are considered the state-of-the-art cathodes for intermediate temperature applications. Indeed, LSCF and BSCF can conduct both electrons and oxygen ions extending the triple-phase-boundary (TPB) in the entire electrode volume.^[8,9,20–25] However, due to the recent geopolitical problems related to Co extraction and commercialization, Co-free materials are intensively studied. Cu is currently under investigation as a substitute.^[26–28] Among all the Cu-based perovskites, lanthanum strontium copper manganite (La_{1-x}Sr_xCu_{1-y}Mn_yO_{3-δ}, LSCuM) is expected to replace La_{1-x}Sr_xMnO₃ for intermediate temperature application. Indeed, the B-site substitution of some Mn atoms with Cu leads to an increase of the Mn⁴⁺, as seen previously for the A-site doping, with an associated increase in electrical conductivity and electrocatalytic activity.^[29–31]

In this work, different core-shell nanofiber electrodes are prepared and tested for application as IT-SOFC cathodes. Ce_{0.9}Gd_{0.1}O_{1.95} (GDC10) fluorite is used as the core material, and different perovskites are used for the shell, namely La_{0.6}Sr_{0.4}MnO₃ (LSM), La_{0.6}Sr_{0.4}Cu_{0.1}Mn_{0.9}O_{3-δ} (LSCuM₁) and La_{0.6}Sr_{0.4}Cu_{0.2}Mn_{0.8}O_{3-δ} (LSCuM₂). Each core-shell nanofiber electrode is characterized through SEM and XRD to investigate the morphological and structural features. Then, the electrochemical characterization is performed through electrochemical impedance spectroscopy (EIS). EIS data are

presented and discussed with reference to previously published results.^[32]

Results and discussion

Morphological and Structural Characterization

Figure 1 shows the SEM images of the core-shell nanofibers after thermal treatment: GDC10/LSM (a–b), GDC10/LSCuM₁ (c–d), and GDC10/LSCuM₂ (e–f). From Figure 1(a,c,e) it is possible to see that the nanofiber tissue appears intact and well entangled in all the samples, providing an interconnected network and therefore continuous paths for both electrons and oxygen ions. Figure 1(b,d,f) highlights the morphology of the single core-shell nanofibers, which is similar in all the samples. SEM images show thin fibers covered by thin veils. Considering the manufacturing process, the thin fibers are recognized as GDC and the thin veils as LSM-based electrocatalyst.

Figure 2 shows the morphology of the core-shell nanofibers after the EIS measurements: GDC10/LSM (a–b), GDC10/LSCuM₁ (c–d), and GDC10/LSCuM₂ (e–f). Compared to Figure 1, the core-shell nanofibers appear slightly broken but the morphology of the nanofibers is still present in all samples. As reported in Figure 2 (e–f), the GDC10/LSCuM₂ shows signs of degradation compared to GDC10/LSCuM₁, where Cu is present in a lower amount. The SEM images suggest an exsolution and/or sintering process, which is likely to be related to the low Cu melting point.

XRD measurements are acquired after heat treatment to check the achievement of the desired crystal phases and the possible presence of secondary phases. In Figure 3 the experimental patterns are reported together with the reference patterns. All the core-shell nanofibers investigated present an experimental pattern that contains all the peaks of the reference La_{0.6}Sr_{0.4}MnO₃ and Ce_{0.9}Gd_{0.1}O_{1.95}. The experimental pattern does not contain additional peaks, therefore, no secondary phases are detected.

In Figure 4, the XRD experimental patterns obtained after the EIS tests are reported. The measurements are carried out on all the cells, to investigate the stability of the materials under working conditions. As shown in Figure 4 all the experimental patterns contain the peaks of the reference La_{0.6}Sr_{0.4}MnO₃ and Ce_{0.9}Gd_{0.1}O_{1.95}, confirming the maintenance of the initial crystal structure. All samples contain some additional peaks which are consistent with the reference pattern of platinum, which is used as a current collector. No other additional peaks are detected, and therefore no secondary phases are formed during the EIS tests.

Electrochemical Characterization

Figure 5 reports the Nyquist and Bode plots of the EIS results obtained from the GDC10/LSM core-shell nanofiber electrode. The measurements are carried out in a temperature range between 550 °C and 850 °C in air. At each temperature, it is

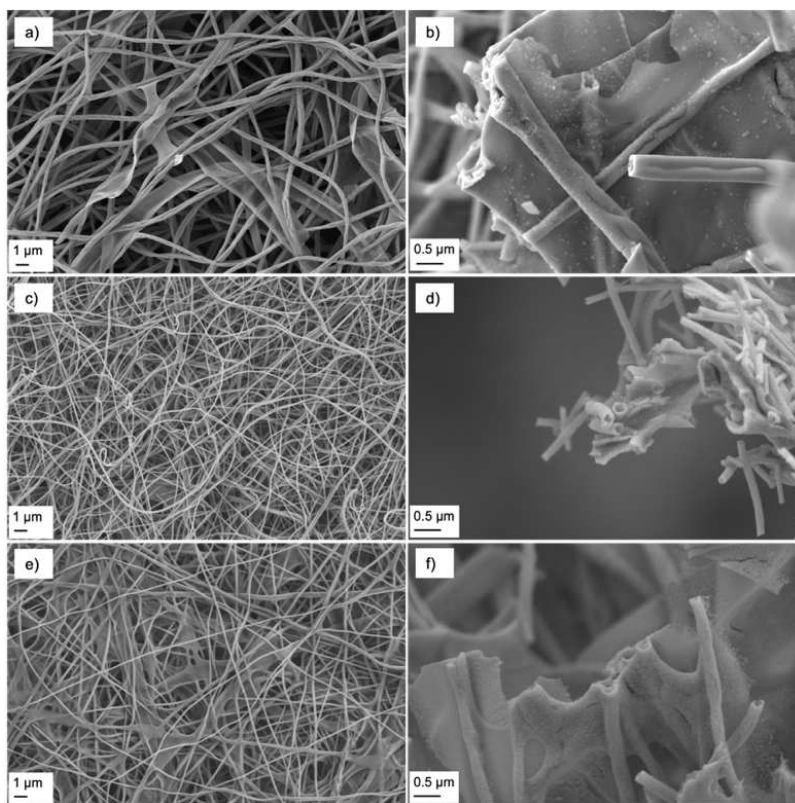


Figure 1. Core-shell nanofibers after heat treatment. (a–b) GDC10/LSM, (b–c) GDC10/LSCuM_1 and (e–f) GDC10/LSCuM_2.

possible to identify two main phenomena, one at high frequency and one at middle-low frequencies. The first is well fitted using only one RQ element, which is named RQ1, whereas the second is fitted with two RQ elements, RQ2 and RQ3 at middle and low frequencies respectively. At the highest testing temperature of 850 °C, RQ2 and RQ3 merge and the fitting is performed using a single RQ element.

The two main arcs shown in Figure 5 are associated with specific processes occurring in the symmetrical cell. The electrochemical behavior reported in Figure 5 is consistent with the results reported in the literature on composite electrodes,^[29,30,32–34] which gives a reference framework for the interpretation. In particular, *Jørgensens and Mogensen* investigated in depth the processes occurring in LSM/YSZ composite cathodes.^[13] They reported that the EIS Nyquist plot for composite LSM/YSZ cathodes can be characterized by the presence of 1–5 arcs. They suggested that the high-frequency arc may be associated with conductivity relaxation phenomena, which are related to the microstructure of the composite.^[13,35] In particular, the transport of the oxygen intermediate, i.e., oxygen ions, across the LSM/YSZ interfaces and the transport of these species through the ionic conductor material inside the composite electrode may generate this high-frequency contribution. The capacity of the RQ element used to fit this experimental arc may be associated with the oxidation and reduction of the Mn ions in the crystal structure of the LSM.^[13] These conclusions are corroborated by several other works,^[36–38] and therefore we suggest that this is also the physical meaning

of the high-frequency arc appearing in Figure 5 and the associated RQ1 fitting element.

As far as the middle-low frequency arc reported in Figure 5 is concerned, it is ascribed to only one phenomenon, even though two separate RQ elements (RQ2 and RQ3) are used to achieve a better fitting of the experimental data and a more precise calculation of the polarization resistance R_p . This middle-low frequency arc reflects the resistances ascribed to the main cathodic process, which consists of the adsorption and dissociation of oxygen molecules on the electrode material surface.^[35] In particular, the process may be dominated by dissociative adsorption, transfer of the species at the TPB, and diffusion through the surface. Thus, the resistance associated with this process greatly depends on the TPB length inside the electrode, and it is generally the main contribution to the overall impedance.^[2,13,35,39]

Despite the presence of both electronic and ionic conductivity inside the core-shell nanofiber electrode, in the EIS results in Figure 5 there is no presence of Gerischer behavior which is well detected in the case of MIECs, i.e. $\text{La}_{1-x}\text{Sr}_x\text{Co}_y\text{Fe}_{1-y}\text{O}_{3-\delta}$.^[21–24,40] This can be inferred from the Nyquist plots in Figure 5, where none of the arcs shows the high-frequency line with a 45° slope typical of Gerischer behavior. In parallel, all the attempts to fit the EIS experimental data with ECs embedding a Gerischer element failed. The non-Gerischer behavior may be explained starting from the morphological properties of composite electrodes. In composite electrodes, the ionic-conduction and the

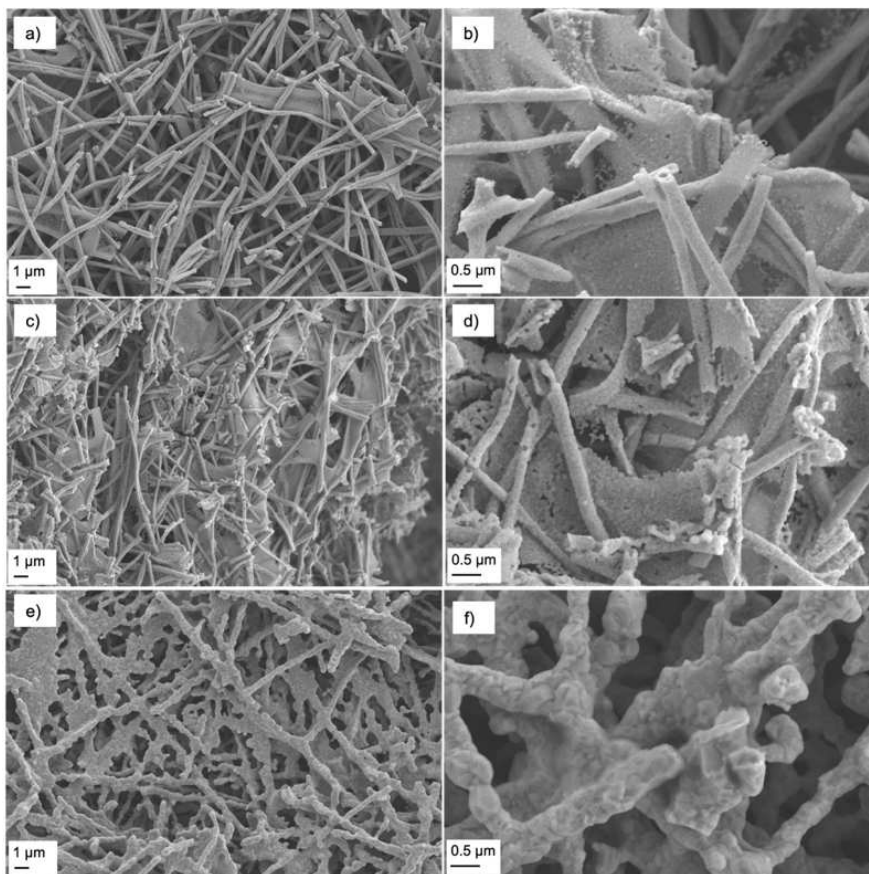


Figure 2. Core-shell nanofibers after the EIS measurements. (a–b) GDC10/LSM, (c–d) GDC10/LSCuM_1 and (e–f) GDC10/LSCuM_2.

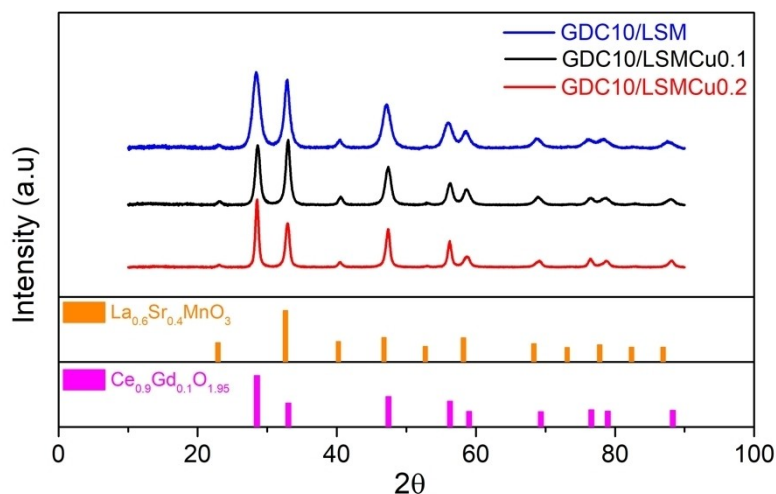


Figure 3. XRD experimental patterns of GDC10/LSM (—), GDC10/LSCuM_1 (—) and GDC10/LSCuM_2 (—) after heat treatment, together with the $\text{La}_{0.6}\text{Sr}_{0.4}\text{MnO}_3$ and $\text{Ce}_{0.9}\text{Gd}_{0.1}\text{O}_{1.95}$ reference peaks.

electronic-conduction paths are placed in two different materials, and the electrochemical reaction can take place only where there is an interfacial connection point between the two materials. Thus, the charge transfer takes place in these active sites and the oxygen ions produced during the reaction follow the ionic path along the ionic conductor

material. This may explain why the EIS response is dominated by multiple RQ arcs, which represent the distributed interfacial active sites along the electrode. On the other hand, in MIECs the two electronic and ionic conduction paths coexist within the same material. Therefore, the ORR can take place in any site along the whole electrode thickness, and the

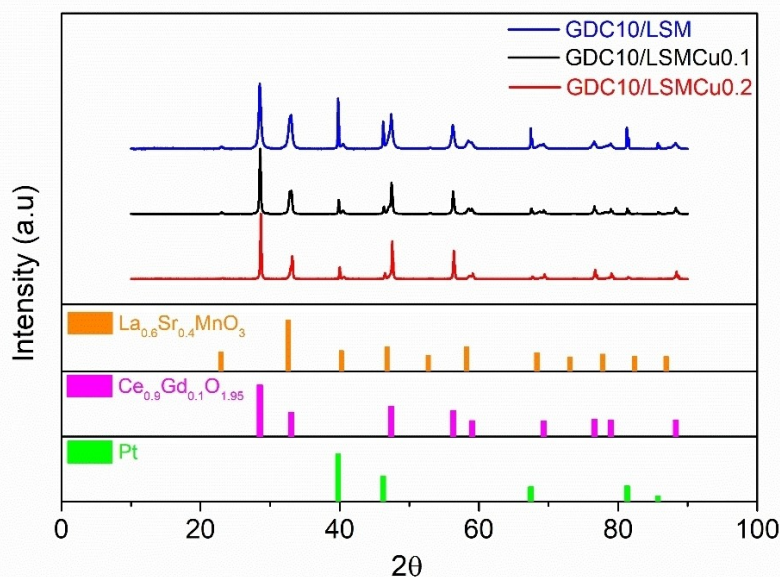


Figure 4. XRD experimental patterns of GDC10/LSM (—), GDC10/LSCuM_1 (—), and GDC10/LSCuM_2 (—) after the EIS measurements, together with the $\text{La}_{0.6}\text{Sr}_{0.4}\text{MnO}_3$, $\text{Ce}_{0.9}\text{Gd}_{0.1}\text{O}_{1.95}$ and Pt reference peaks.

oxygen ions produced during the electrochemical reaction follow the ionic path which is in the same material. In other words, electron and ion conduction occur inside the same material together with distributed electrochemical reaction, which is the necessary condition for the Gerischer to manifest itself in the EIS experimental results. A schematic representation of the electrochemical reaction in composite and MIEC electrodes is reported in Figure 6.

The EIS measurements reported in Figure 5 are then used to calculate the polarization resistance R_p of the GDC10/LSM core-shell nanofiber electrode. R_p is around $2 \Omega \text{cm}^2$ at 700°C and $R_p \sim 0.28 \Omega \text{cm}^2$ at 850°C . Murray and Barnett investigated $\text{La}_{0.8}\text{Sr}_{0.2}\text{MnO}_3\text{-Ce}_{0.8}\text{Gd}_{0.2}\text{O}_{2-x}$ composite powder-based electrodes and found $R_p \sim 6.5 \Omega \text{cm}^2$ at 700°C ,^[34] whereas Sanna *et al.* found an R_p around $5 \Omega \text{cm}^2$ at the same operating temperature with LSM/GDC10 composite powder-based electrodes.^[32] Noh *et al.* investigated $\text{La}_{0.8}\text{Sr}_{0.2}\text{MnO}_3\text{-Ce}_{0.8}\text{Gd}_{0.2}\text{O}_{2-x}$ powder-based electrode as well, and they found $R_p \sim 1.5 \Omega \text{cm}^2$ at 700°C .^[29] At 850°C , the literature on composite powder-based electrodes reports values in the order of $R_p \sim 0.36 \Omega \text{cm}^2$ ^[29] up to $1 \Omega \text{cm}^2$.^[32] Therefore, the GDC10/LSM core-shell nanofiber cathodes appear promising for low and intermediate-temperature SOFCs.

In a further development step, Cu doping was performed to increase the electrocatalytic activity of LSM. Figure 7 and Figure 8 show the EIS results obtained respectively for GDC10/LSCuM_1 and GDC10/LSCuM_2 core-shell nanofiber electrodes. The EIS measurements are carried out in a temperature range between 550°C and 850°C in an air atmosphere. The GDC10/LSCuM_1 experimental data are fitted using the RQ1-RQ2-RQ3 equivalent circuit between 550°C and 600°C , whereas above 600°C only two RQs are

used. Furthermore, at 800°C and 850°C , the FLW element is added to fit the low-frequency arc associated with gas transport limitations. As discussed in previous works,^[23,41] this arc shows little temperature dependence, and at low temperature it is practically not visible because it is very small compared to the other impedance arcs. At high temperatures, however, all the other arcs are reduced and the diffusive arc becomes visible. The GDC10/LSCuM_2 EIS results are fitted through the same RQ1-RQ2-RQ3 equivalent circuit at all the operating temperatures, except for 850°C where only two RQs are employed. The ECs used for GDC10/LSCuM_1 and GDC10/LSCuM_2 are consistent with the literature.^[29,30]

The GDC10/LSCuM_2 Nyquist plots shown in Figure 8 appear very similar to the GDC10/LSM results reported in Figure 5. On the contrary, the GDC10/LSCuM_1 Nyquist plots reported in Figure 7 are slightly different compared to the GDC10/LSM graphs. Indeed, the GDC10/LSCuM_1 two main arcs are partially superimposed, especially at high temperatures.

As far as the electrochemical performance is concerned, the polarization resistance R_p achieved with the GDC10/LSCuM_1 and GDC10/LSCuM_2 core-shell nanofiber cathodes appears interesting. Indeed, the Cu-based perovskite materials show better performance at all the temperatures investigated. In particular, at 700°C the polarization resistances of the GDC10/LSCuM_1 and GDC10/LSCuM_2 core-shell nanofiber cathodes are around $0.9 \Omega \text{cm}^2$ and $0.8 \Omega \text{cm}^2$ respectively. These values are remarkably lower compared to the R_p of the GDC10/LSM core-shell nanofiber cathodes, which is $2 \Omega \text{cm}^2$. This confirms the expected effectiveness of Cu in improving the electrocatalytic performance of LSM-based electrodes. Furthermore, GDC10/LSCuM_1 and GDC10/LSCuM_2 core-shell nanofiber

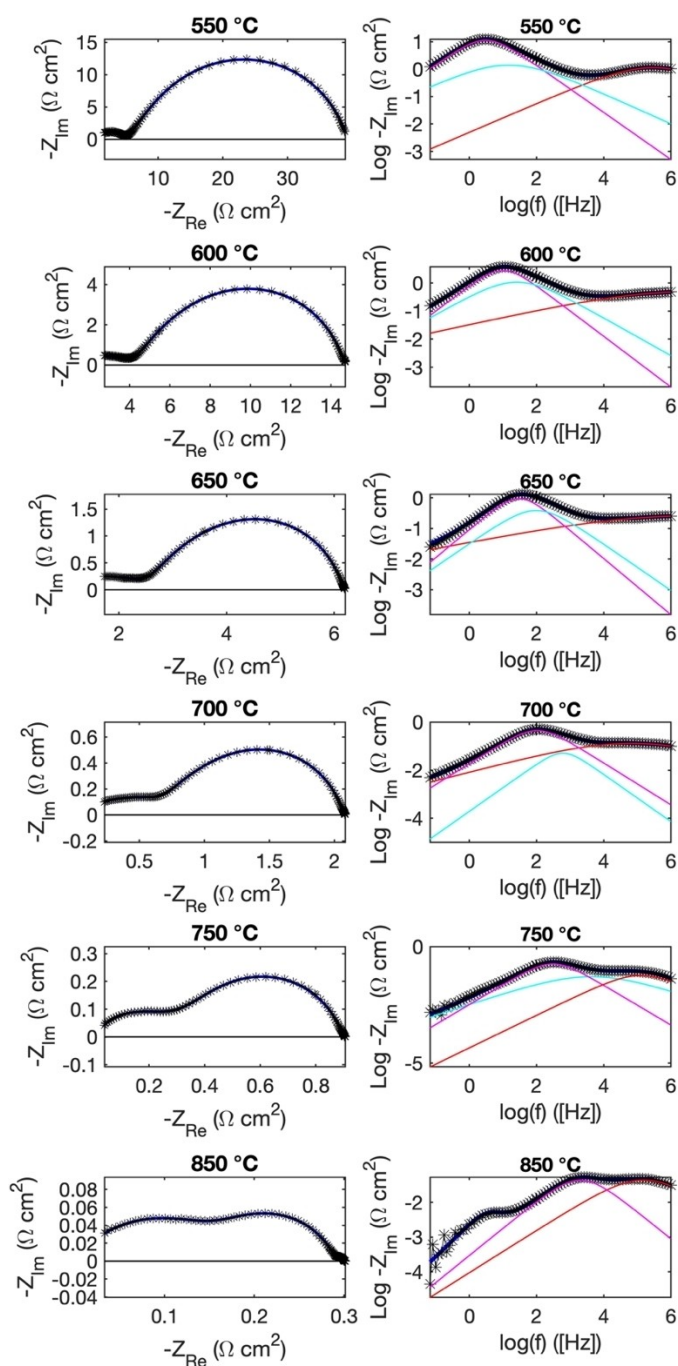


Figure 5. Nyquist (left) and Bode (right) plots of the EIS measurements on the GDC10/LSM core-shell nanofiber electrode at temperatures from 550 °C to 850 °C, in air atmosphere: *experimental data; — fitting through the R_s -RQ1-RQ2-RQ3 equivalent circuit model; — RQ1 contribution; — RQ2 contribution; — RQ3 contribution (vanishing at 850 °C).

cathodes show better performance compared with the literature values, where a polarization resistance around $1.3 \Omega \text{ cm}^2$ is reported for the GDC10/LSCuM_1 and LSCuM_2/ powder-based electrodes.^[29] This further demonstrates the ability of the innovative electrospun core-shell nanofibers to improve electrode performance.

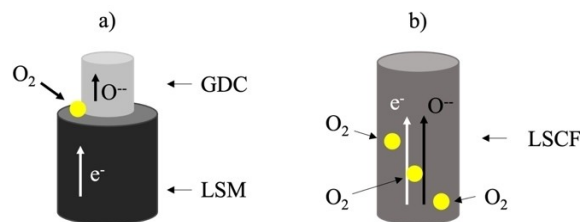


Figure 6. The charge transfer process in composite (a) and MIEC (b) cathodes. The • represents the reaction active site.

Figure 9 shows the Arrhenius plot of the reciprocal polarization resistance R_p^{-1} for the core-shell nanofiber cathodes investigated. It is possible to see that all the core-shell nanofiber electrodes have better performance than the reference powder-based LSM/GDC10 composite cathode, which consists of a cathode made with crushed LSM nanofibers mixed with GDC10 powders.^[32] In particular, the GDC10/LSCuM_1 and GDC10/LSCuM_2 core-shell nanofiber electrodes outperform both the GDC10/LSM core-shell nanofiber cathode and the reference powder-based LSM/GDC10 composite cathode. Furthermore, Figure 9 reports the activation energy E_A calculated for all the electrodes investigated. It is possible to see that the addition of Cu to the LSM perovskite results in a decrease in the activation energy of the overall polarization resistances. In particular, the GDC10/LSCuM_2 core-shell nanofiber cathodes report the lowest value of E_A (106 kJ/mol) and the lowest values of R_p at low temperatures, even if very close to the GDC10/LSCuM_1 core-shell nanofibers. Nevertheless, as already discussed and displayed in Figure 2, the higher the amount of Cu in the perovskite, the higher the degradation during the EIS measurements. Hence, the GDC10/LSCuM_1 core-shell nanofiber cathodes appear preferable since they guarantee reduced degradation and higher morphological stability.

Figure 10 reports the Arrhenius plot of the polarization resistances associated with the RQ1 EC element, reflecting respectively the high-frequency processes. It is very interesting to see that the resistances $R_{p,RQ1}$, and their activation energies E_A , are similar for all the core-shell nanofibers investigated in this work, and also similar to the powder-based LSM/GDC10 electrode.^[32] E_A is around 90 kJ/mol, which is consistent with literature values.^[35] The agreement between the activation energies E_A of the high-frequency processes for all the electrodes studied in this work supports the hypothesis that the underlying physical meaning is the same.

Figure 11 reports the Arrhenius plot of the polarization resistances associated with the (RQ2 + RQ3) EC elements, reflecting the low-medium frequency processes, which, as already remarked, strongly depend on the TPB length inside the electrode. Also in this case, the activation energy E_A of $R_{p,(RQ2+RQ3)}^{-1}$ is similar for all the core-shell nanofibers. The E_A value is about 140 kJ/mol for the GDC10/LSM core-shell nanofibers and decreases as the amount of Cu inside the perovskite increases. Again, the activation energy is consistent with the value reported in the literature for low-medium frequency phenomena.^[13] Once more, the agreement be-

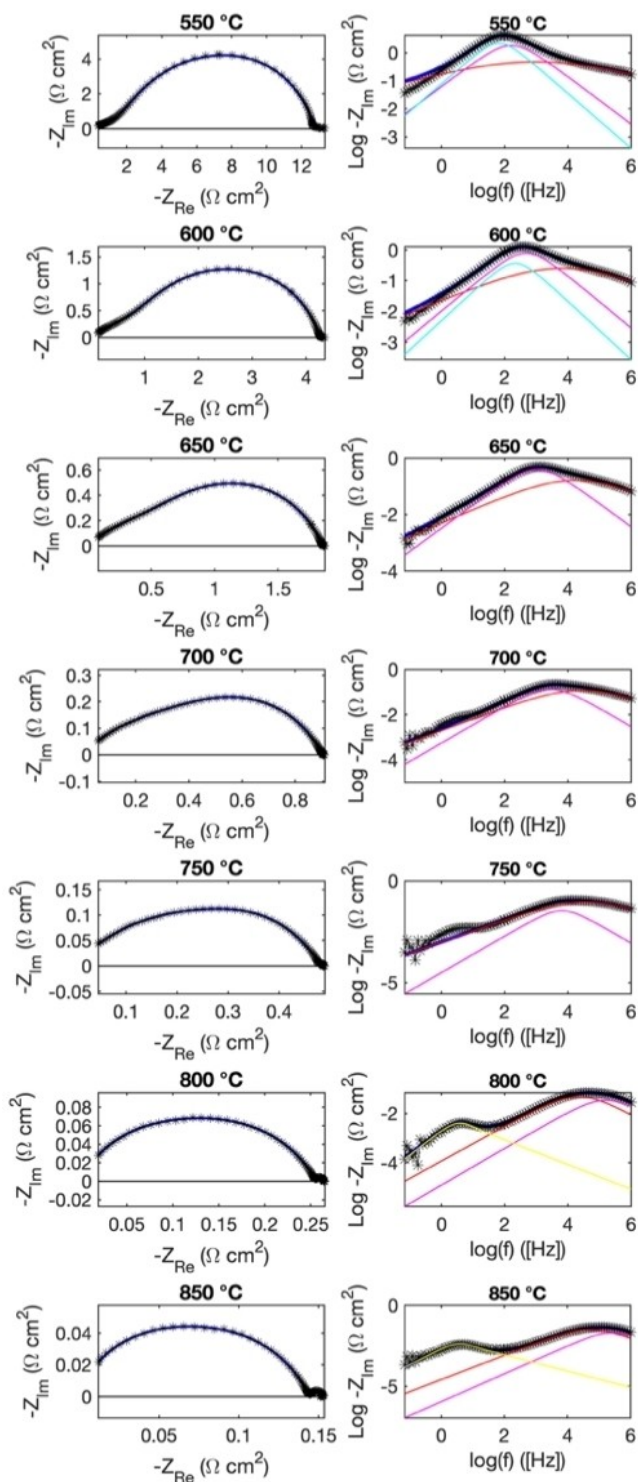


Figure 7. Nyquist (left) and Bode (right) plots of the EIS measurements on the GDC10/LSCuM_1 core-shell nanofiber electrode at temperatures from 550 °C to 850 °C, in air atmosphere: *experimental data; — fitting through the Rs-RQ1-RQ2-RQ3 equivalent circuit model; — RQ1 contribution; — RQ2 contribution; — RQ3 contribution (vanishing at 650 °C); — FLW (appearing at 800 °C).

tween the activation energy E_a of the low-medium frequency processes for all the core-shell nanofiber electrodes studied in this work supports the hypothesis that the underlying

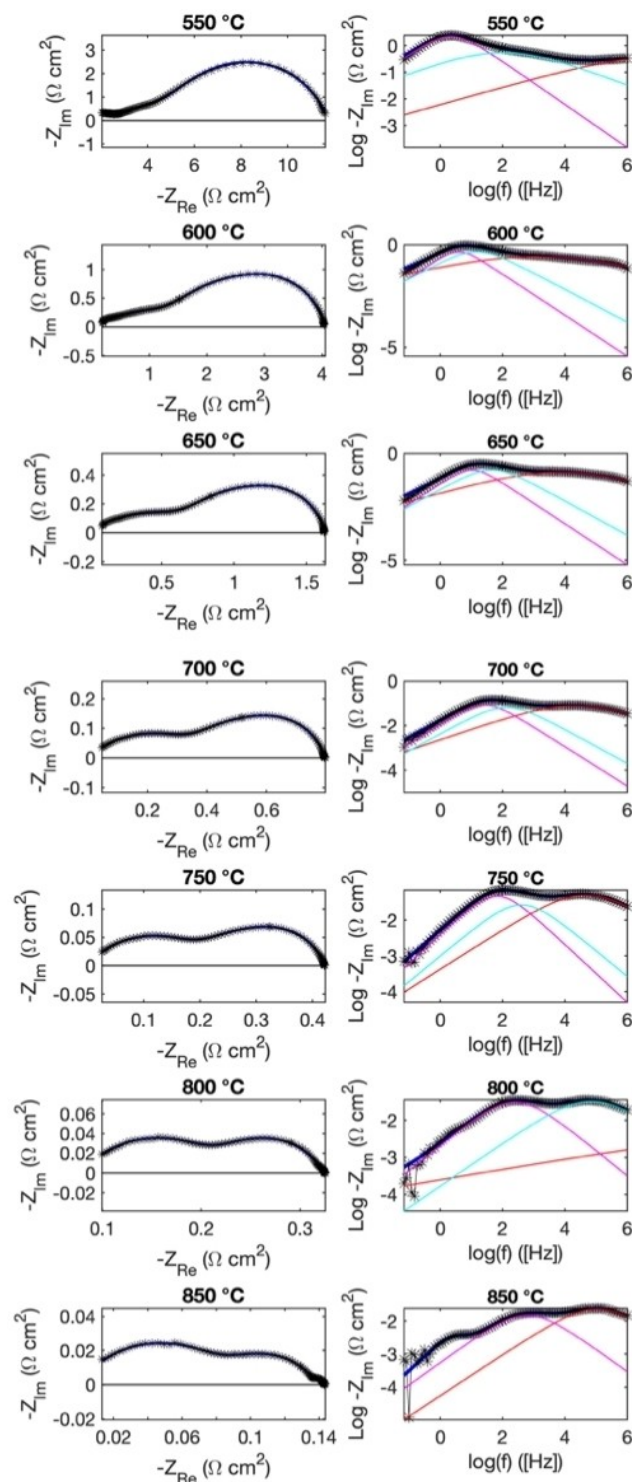


Figure 8. Nyquist (left) and Bode (right) plots of the EIS measurements on the GDC10/LSCuM_2 core-shell nanofiber electrode at temperatures from 550 °C to 850 °C, in air atmosphere: *experimental data; — fitting through the Rs-RQ1-RQ2-RQ3 equivalent circuit model; — RQ1 contribution; — RQ2 contribution; — RQ3 contribution (vanishing at 800 °C).

physical meaning is the same. Nevertheless, even if the activation energies are similar, the polarization resistances $R_{p,(RQ2+RQ3)}$ associated with the low-medium frequency process

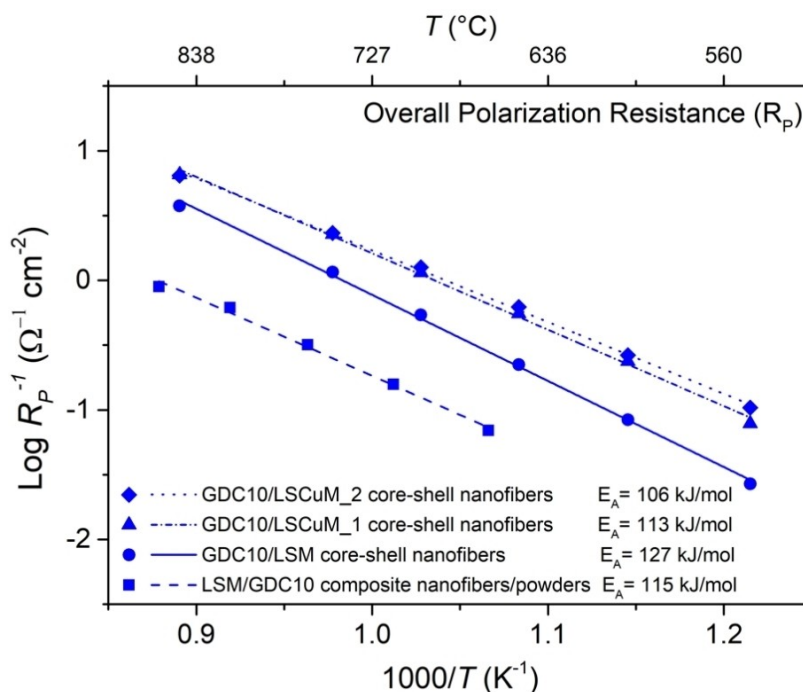


Figure 9. Arrhenius plot of R_p^{-1} for GDC10/LSM, GDC10/LSCuM_1, and GDC10/LSCuM_2 core-shell nanofiber cathodes. These are compared with the LSM/GDC10 composite nanofiber/powder electrode (LSM nanofibers mixed with GDC10 powders).^[32]

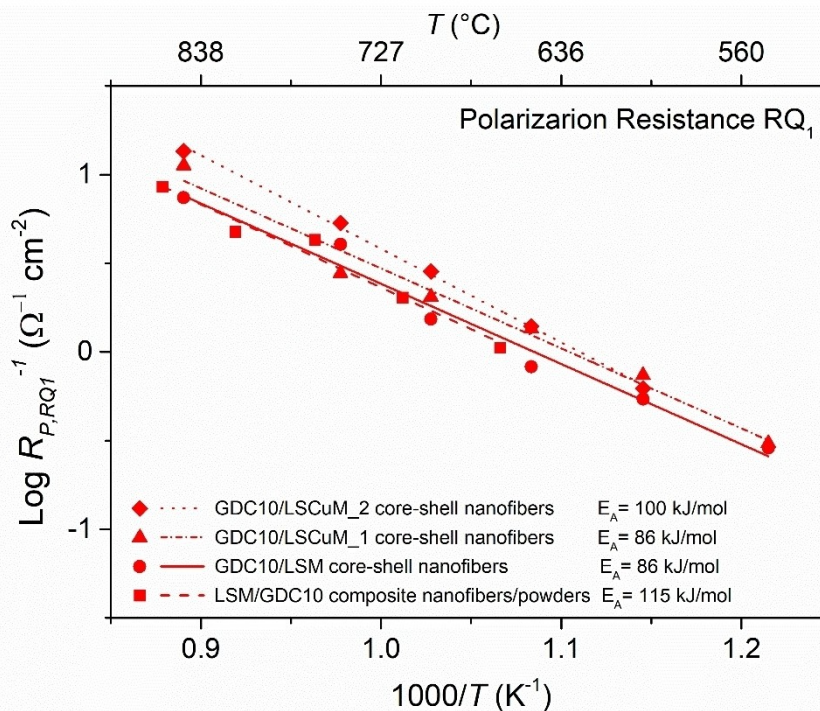


Figure 10. Arrhenius plot of $R_{p,RQ1}^{-1}$ of GDC10/LSM, GDC10/LSCuM_1 and GDC10/LSCuM_2 core-shell nanofiber cathodes. These are compared with the LSM/GDC10 composite nanofiber/powder electrode (LSM nanofibers mixed with GDC10 powders).^[32]

(electrochemical reaction) are different in the samples investigated. Considering the LSM/GDC10 composite nanofiber/powder electrode as the baseline, then the GDC10/LSM

shows significant improvement. Since the materials are the same, the difference must be related to the different TPB length in the two samples, demonstrating that core-shell

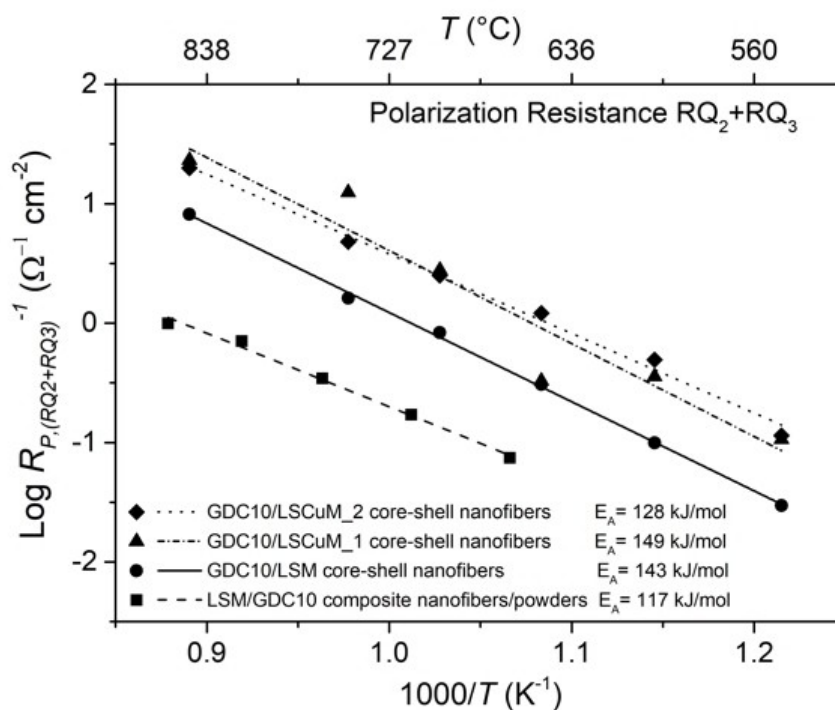


Figure 11. Arrhenius plot of $R_{p,(RQ_2+RQ_3)}^{-1}$ of GDC10/LSM, GDC10/LSCuM_1 and GDC10/LSCuM_2 core-shell nanofiber cathodes. These are compared with the LSM/GDC10 composite nanofibers/powders electrode (LSM nanofibers mixed with GDC10 powders).^[32]

electrospinning is effective in increasing the TPB length over that of powder composites. Hence, the further improved performance of GDC10/LSCuM_1 and GDC10/LSCuM_2 core-shell nanofiber cathodes can be ascribed to the improvement in electrocatalytic activity caused by Cu.

Conclusions

Preparation and electrochemical characterization of GDC10/LSM, GDC10/LSCuM_1, and GDC10/LSCuM_2 core-shell nanofiber electrodes are investigated for possible application at the cathode side of IT-SOFCs. XRD experimental patterns collected before and after the electrochemical tests reveal that no secondary phases are detected in any of the core-shell nanofibers. EIS experimental data and EC modeling confirm the absence of Gerischer behavior, which is typically found with MIEC materials such as LSCF and BSCF. Instead, an RQ-based EC fits perfectly the EIS experimental data. This suggests that only MIEC electrodes featuring electronic/ionic conductivity and electrochemical reaction inside the same material display a Gerischer element in the EIS experimental data. Conversely, in composite electrodes, where electronic and ionic conduction occur in two different materials with the electrochemical reaction at the interface, the EIS response is dominated by the RQ elements associated with the interfacial charge transfer reaction.

The GDC10/LSM core-shell nanofiber electrode shows a polarization resistance $R_p \sim 1.9 \Omega \text{ cm}^2$ at 700°C , significantly

lower compared to that of powder-based electrodes (around $6.3 \Omega \text{ cm}^2$ at 715°C). This improvement is ascribed to the continuous connection between the ionic conductor fluorite (core) and the electronic conductor perovskite (shell). This promotes the formation of a large number of reaction sites, which are located in every part of the core-shell nanofiber and extend the TPB into the entire electrode thickness. In a further development step, Cu-doping at the B-site of the LSM crystal structure is tested. The core-shell nanofiber electrodes with 0.1 molar Cu-doped LSM (GDC10/LSCuM_1), have $R_p \sim 0.9 \Omega \text{ cm}^2$ at 700°C . Similarly, the core-shell nanofiber electrodes with 0.2 molar Cu-doped LSM (GDC10/LSCuM_2), have $R_p \sim 0.8 \Omega \text{ cm}^2$ at 700°C . Both values are less than 50% of the R_p of GDC10/LSM core-shell nanofibers at the same temperature. Therefore, it can be concluded that Cu-doping improves the electrocatalytic properties. Nevertheless, SEM images of the GDC10/LSCuM_2 after the EIS test show degradation, which is not detected for GDC10/LSCuM_1. In conclusion, in the system of Cu-doped LSM perovskites, the LSCuM_1 stoichiometry, corresponding to a Cu doping of 0.1 molar, is proposed here as the most promising material to be used on the shell side, in combination with a GDC10 core, in core-shell nanofiber cathodes for IT-SOFCs.

Experimental Section

Core-Shell Nanofiber Preparation

Core-shell nanofibers consist of an inner ionic conductor nanofiber (core) covered by an electrocatalyst nanofiber (shell). Gadolinium doped Ceria ($\text{Ce}_{0.9}\text{Gd}_{0.1}\text{O}_{1.95}$, GDC10) is the core material of all the nanofibers, whereas three different shell materials are investigated: $\text{La}_{0.6}\text{Sr}_{0.4}\text{MnO}_3$ (LSM), $\text{La}_{0.6}\text{Sr}_{0.4}\text{Cu}_{0.1}\text{Mn}_{0.9}\text{O}_{3-\delta}$ (LSCuM_1) and $\text{La}_{0.6}\text{Sr}_{0.4}\text{Cu}_{0.2}\text{Mn}_{0.8}\text{O}_{3-\delta}$ (LSCuM_2). Core-shell nanofibers need two separate starting solutions, containing the precursors of the core and shell materials. The metal salts used in this work are $\text{La}(\text{NO}_3)_3 \cdot 6\text{H}_2\text{O}$ (AlfaAesar, 99.9%), $\text{Sr}(\text{NO}_3)_2$ (Sigma-Aldrich, ACS 99+%), $(\text{CH}_3\text{COO})_2\text{Mn} \cdot 4\text{H}_2\text{O}$ (Sigma-Aldrich, 99.99%), $\text{Cu}(\text{NO}_3)_2 \cdot 3\text{H}_2\text{O}$ (Sigma-Aldrich, p.a., 99–104%), $\text{Gd}(\text{NO}_3)_3 \cdot 6\text{H}_2\text{O}$ (Sigma-Aldrich 99.9%), $\text{Ce}(\text{NO}_3)_3 \cdot 6\text{H}_2\text{O}$ (Sigma-Aldrich 99.99%). For all the solutions, polyvinylpyrrolidone (PVP, $M_w = 1.3 \cdot 10^6$ g/mol, Sigma-Aldrich) is added as carrier polymer and N–N-Dimethylformamide (DMF, Sigma-Aldrich, ACS, >99.8) is selected as solvent. The salts are added to each solution to achieve the proper stoichiometry, which, for the shell materials, is reported in Table 1.

As far as the GDC10 stoichiometry is concerned, the Ce:Gd mole ratio is 0.9:0.1. In the core starting solution, the PVP ratio is 11.5% wt/wt, whereas in the shell starting solutions PVP is 13% wt/wt.

The electrospinning equipment used for the core-shell nanofiber preparation process is provided by Doxa Microfluids, equipped with a 10 ml syringe and two co-axial needles whose diameters are 0.8 mm and 0.4 mm. All the core-shell nanofibers are ejected with a flow rate of 1 mL/h, and an applied voltage of 2.4 kV/cm. The rotational speed is 200 rpm, and the relative humidity inside the chamber is maintained at 40%. Then, all the raw core-shell nanofiber tissues are cut in a circular shape and heat-treated. The raw core-shell nanofibers reach 800 °C as the maximum temperature, with a heating ramp of 60 °C/h. Between 350 °C and 500 °C, the heating ramp is set at 12 °C/hour to prevent the gas released by the degradation of the polymer from damaging the structure of the nanofibers. Once the maximum temperature is reached, the samples are cooled down at 60 °C/h. During heat treatment, a uniform shrinkage takes place, reducing the initial diameter by about 50%. The heat-treated electrode thickness is in the order of 70 μm. Electrode diameter and area are reported in Table 2.

Symmetrical Cell Preparation

Electrolyte disks are prepared by pressing the GDC10 powder supplied by Fuelcellmaterials (GDC10-TC powder, particle size 0.1–0.4 μm, surface area 5.9 m²/g). Uniaxial pressing is carried out by filling the die body from the bottom, achieving a high uniformity,

Table 1. Mole ratio between the perovskite elements of the electrocatalyst investigated.				
	La:Sr	Cu:Fe	Cu:Mn	Mn
LSM	6:4	[-:-]	[-:-]	1
LSCuM_1	6:4	[-:-]	1:9	[-:-]
LSCuM_2	6:4	[-:-]	2:8	[-:-]

Table 2. Core-shell nanofiber electrode dimension.		
	Diameter [cm]	Area [cm ²]
LSM	0.79	0.48
LSCuM_1	0.77	0.46
LSCuM_2	0.76	0.45

and thus obtaining a high-density sintered electrolyte. The electrolytes are prepared using a pressing force of 5 tons. Then, the electrolytes are sintered with a maximum temperature of 1300 °C. The electrolyte thickness is in the order of 1 mm. The cells are assembled symmetrically attaching the heat-treated electrodes on both sides of the electrolyte disks, using a droplet of GDC10 electrospinning solution as a glue. The complete symmetrical cells are fired at 950 °C for 2 hours, using a thermal ramp of 60 °C/h both during heating and cooling. Lastly, a thin layer of platinum is placed onto each electrode to function as a current collector.

Morphological and Structural Characterization

The morphology of core-shell nanofiber electrodes is investigated through scanning electron microscopy (SEM). SEM images are acquired after both the thermal treatment and the EIS test, to investigate degradation. The SEM instrument is Zeiss Merlin, and image acquisition is carried out with the SE detector, using an acceleration voltage of 5 kV. Nanofiber composition is evaluated through X-ray diffraction (XRD) analysis. The measurements are carried out both before and after the EIS test, through a Malvern Panalytical AERIS using a Cu K α radiation, an acceleration voltage of 40 kV, and a filament current of 15 mA.

Electrochemical Test Set-Up

Electrochemical characterization is performed using electrochemical impedance spectroscopy (EIS). All the symmetrical cells are fixed between two platinum meshes, ensuring stable contact with the thin layers of platinum deposited onto each electrode surface. Then, a sintering process is carried out in situ at 850 °C, to enhance platinum adhesion. The EIS measurements are carried out at 850 °C, 750 °C, 700 °C, 650 °C, 600 °C, and 550 °C, in air atmosphere. Since microstructure modifications occur faster at high temperature, the tests reported in the paper have been performed starting from high temperature and then decreasing to low temperature, in order to ensure as much as possible that all the tests are performed with the same microstructure. The instrument used to acquire the EIS data is a Solartron 1260, setting a frequency range between 0.01 Hz and 10⁶ Hz with 10 mV of amplitude and collecting 10 measurements per decade. The data are then corrected to subtract the contributions of the device, which consist of an inductance and a capacity, respectively of the order of $L = 10^{-7}$ H and $C = 10^{-10 \div -9}$ F.

Equivalent Circuit-Based Modeling of Electrochemical Impedance Spectroscopy Data

The EIS experimental data are fitted through the L-RsC-RQ1-RQ2-RQ3(-FLW) equivalent circuit (EC), which is similar to the EC model proposed in previous work.^[32] The fitting parameters obtained for all the samples investigated are reported in Table S11. The inductance L and the C element do not contribute to simulating the electrochemical phenomena occurring in the electrode, but they are associated with the electrochemical test apparatus and the arrangement of the wires. The corresponding impedance contributions are subtracted from both the experimental data and the fittings reported subsequently in this work. Therefore, the EC will be referred to as Rs-RQ-RQ-RQ(-FLW). Rs is a resistor, which accounts for the electrolyte ohmic resistance, the contact resistances between the different layers, and the two electrodes' ohmic resistances, the latter being normally negligible (Eq. 1).

$$R_s = R_{\text{electrolyte}} + 2(R_{\text{contact}} + R_{\text{electrode}}) \quad (1)$$

The RQ element consists of a resistor in parallel with a constant phase element (CPE). This element is used to simulate the electrochemical processes which take place at the interface between the electronic and the ionic conductor.^[35,42] The charge transfer process, which is the oxygen reduction reaction (ORR) at the cathode side of the fuel cell, is simulated by the resistor, whereas for the electrode/electrolyte double layer the Q element is used. The RQ impedance equation is given by Eq. 2 below:

$$Z_{RQ}(\omega) = \frac{1}{R_{RQ}^{-1} + Q(j\omega)^\alpha} \quad (2)$$

Where α is a frequency-independent parameter of the CPE. When $\alpha = 1$, the CPE becomes an ideal capacitor, with capacity Q and unit (F), and the impedance is a semi-circle in the Nyquist plot. When α is lower than 1, the CPE is a non-ideal capacitor and the RQ impedance reflects its deviation from ideality. For example, the surface heterogeneities at the interface between electronic and ionic conductors, or continuously distributed time constants for the charge-transfer reactions, affect the α value.^[43] The Q unit becomes ($Fs^{\alpha-1}$), and therefore an equivalent capacitance Q_{equiv} , which has (F) as the unit, is calculated according to Eq. 3 below:

$$Q_{equiv} = \frac{(QR)^{1/\alpha}}{R} \quad (3)$$

When the electrochemical measurements are carried out at high temperatures, an RQ element disappears from the EC used for fitting the data, with the transition temperature being different for each sample. Furthermore, the gas limitation phenomena start to give a considerable contribution to the overall polarization resistance. Therefore, an additional arc appears at low frequencies, which is well fitted by the Finite-Length-Warburg (FLW) circuit element. The mathematical expression of the FLW circuit element is given by Eq. 4.^[41]

$$Z_{FLW}(\omega) = \frac{\tanh((Bj\omega)^{0.5})}{(Yj\omega)^{0.5}} \quad (4)$$

Where B and Y are phenomenological coefficients.

Finally, the polarization resistance R_p is evaluated from the fittings as the difference between the low and high frequency intercepts of the Nyquist impedance spectra with the real axis. Furthermore, since this process can also be applied also to individual elements of the EC, a separate R_p is defined for each EC element.^[23,42,44]

Acknowledgment

The group at the University of Genoa, Italy, acknowledges financial support from the Compagnia di San Paolo Project 'COELUS – Production of renewable fuel by CO-Electrolysis and reUse of carbon dioxide' (ID ROL 32604). Mohamad Koshkalam is gratefully acknowledged for his contribution to the electrochemical tests carried out at the Technical University of Denmark.

Conflict of Interests

The authors declare no conflict of interest.

Data Availability Statement

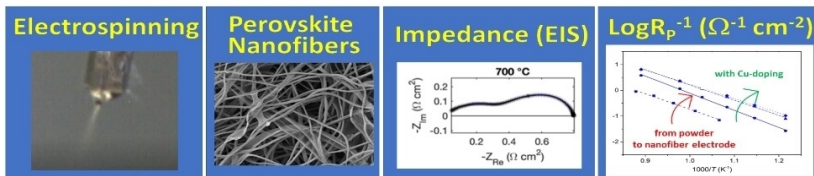
The data that support the findings of this study are available from the corresponding author upon reasonable request.

Keywords: cathode · electrospinning · electrochemical impedance spectroscopy (EIS) · perovskite · solid oxide fuel cell (SOFC)

- [1] G. Yang, W. Jung, S. J. Ahn, D. Lee, *Appl. Sci.* **2019**, *9*, 1030.
- [2] S. P. Jiang, *J. Mater. Sci.* **2008**, *43*, 6799–6833.
- [3] P. Costamagna, P. Holtappels, C. Sanna, in *Metal Oxide-Based Nanofibers and Their Applications*, Elsevier, Amsterdam, **2021**, pp. 301–331.
- [4] A. Bertei, G. Arcolini, J. P. Ouweltjes, Z. Wuillemin, P. Piccardo, C. Nicolella, *Electrochim. Acta* **2016**, *208*, 129–141.
- [5] A. Enrico, B. Aliakbarian, A. Lagazzo, A. Donazzi, R. Botter, P. Perego, P. Costamagna, *Fuel Cells* **2017**, *17*, 415–422.
- [6] S. T. Aruna, L. S. Balaji, S. S. Kumar, B. S. Prakash, *Renewable Sustainable Energy Rev.* **2017**, *67*, 673–682.
- [7] Y. Chen, Y. Bu, Y. Zhang, R. Yan, D. Ding, B. Zhao, S. Yoo, D. Dang, R. Hu, C. Yang, M. Liu, *Adv. Energy Mater.* **2017**, *7*, 1–7.
- [8] E. Zhao, Z. Jia, L. Zhao, Y. Xiong, C. Sun, M. E. Brito, *J. Power Sources* **2012**, *219*, 133–139.
- [9] A. Enrico, W. Zhang, M. Lund Traulsen, E. M. Sala, P. Costamagna, P. Holtappels, *J. Eur. Ceram. Soc.* **2018**, *38*, 2677–2686.
- [10] M. J. L. Østergård, C. Clausen, C. Bagger, M. Mogensen, *Electrochim. Acta* **1995**, *40*, 1971–1981.
- [11] J. Nielsen, J. Hjelm, *Electrochim. Acta* **2014**, *115*, 31–45.
- [12] S. P. Jiang, J. G. Love, J. P. Zhang, M. Hoang, Y. Ramprakash, A. E. Hughes, S. P. S. Badwal, *Solid State Ionics* **1999**, *121*, 1–10.
- [13] M. J. Jørgensen, M. Mogensen, *J. Electrochem. Soc.* **2001**, *148*, A433.
- [14] S. Wang, X. Lu, M. Liu, *J. Solid State Electrochem.* **2002**, *6*, 384–390.
- [15] T. Kenjo, S. Osawa, K. Fujikawa, *J. Electrochem. Soc.* **1991**, *138*, 349–355.
- [16] P. Tanasini, M. Cannarozzo, P. Costamagna, A. Faes, J. Van Herle, A. Hessler-Wyser, C. Comninellis, *Fuel Cells* **2009**, *9*, 740–752.
- [17] P. Costamagna, P. Costa, V. Antonucci, *Electrochim. Acta* **1998**, *43*, 375–394.
- [18] P. Costamagna, P. Costa, E. Arato, *Electrochim. Acta* **1998**, *43*, 967–972.
- [19] Y. Jeon, J. Myung, S. Hyun, Y. Shul, J. T. S. Irvine, *J. Mater. Chem. A* **2017**, *5*, 3966–3973.
- [20] V. C. Kournoutis, F. Tietz, S. Bebelis, *Fuel Cells* **2009**, *9*, 852–860.
- [21] P. Costamagna, C. Sanna, A. Campodonico, E. M. Sala, R. Sažinas, P. Holtappels, *Fuel Cells* **2019**, *19*, 472–483.
- [22] C. Sanna, W. Zhang, P. Costamagna, P. Holtappels, *Int. J. Hydrogen Energy* **2021**, *46*, 13818–13831.
- [23] P. Costamagna, E. M. Sala, W. Zhang, M. Lund Traulsen, P. Holtappels, *Electrochim. Acta* **2019**, *319*, 657–671.
- [24] S. P. Jiang, *Int. J. Hydrogen Energy* **2019**, *44*, 7448–7493.
- [25] N. T. Hieu, J. Park, B. Tae, *Mater. Sci. Eng. B* **2012**, *177*, 205–209.
- [26] J. Bai, Z. Han, B. Lv, X. Chen, X. Zhu, D. Zhou, *Int. J. Hydrogen Energy* **2021**, *46*, 8132–8142.
- [27] G. Coffey, J. Hardy, O. Marina, L. Pederson, P. Rieke, E. Thomsen, *Solid State Ionics* **2004**, *175*, 73–78.
- [28] A. Berenov, H. Wood, A. Atkinson, *J. Electrochem. Soc.* **2007**, *154*, B1362.
- [29] T. Noh, H. Lee, *J. Solid State Electrochem.* **2014**, *18*, 613–619.
- [30] T. Noh, J. Ryu, R. O'Hayre, H. Lee, *Solid State Ionics* **2014**, *260*, 30–35.
- [31] Y. Chen, H. Hu, N. Wang, B. Sun, M. Yao, W. Hu, *Chem. Eng. J.* **2020**, *391*, 123536.
- [32] C. Sanna, E. Squizzato, P. Costamagna, P. Holtappels, A. Glisenti, *Electrochim. Acta* **2022**, *409*, 139939.
- [33] K. Chen, N. Ai, S. P. Jiang, *Int. J. Hydrogen Energy* **2014**, *39*, 10349–10358.
- [34] E. Perry Murray, S. A. Barnett, *Solid State Ionics* **2001**, *143*, 265–273.
- [35] E. Barsoukov, J. R. Macdonald, *Impedance Spectroscopy: Theory, Experiment, and Applications*, John Wiley & Sons, Hoboken, New Jersey, **2005**.
- [36] E. P. Murray, T. Tsai, S. A. Barnett, *Solid State Ionics* **1998**, *110*, 235–243.
- [37] J. Nielsen, T. Jacobsen, M. Wandel, *Electrochim. Acta* **2011**, *56*, 7963–7974.

- [38] T. Suzuki, M. Awano, P. Jasinski, V. Petrovsky, H. U. Anderson, *Solid State Ionics* **2006**, *177*, 2071–2074.
- [39] S. B. Adler, J. A. Lane, B. C. H. Steele, *J. Electrochem. Soc.* **1996**, *143*, 3554–3564.
- [40] J. Chen, F. Liang, B. Chi, J. Pu, S. P. Jiang, L. Jian, *J. Power Sources* **2009**, *194*, 275–280.
- [41] T. Jacobsen, P. V. Hendriksen, S. Koch, *Electrochim. Acta* **2008**, *53*, 7500–7508.
- [42] M. E. Orazem, N. Pébère, B. Tribollet, *J. Electrochem. Soc.* **2006**, *153*, B129.
- [43] M. E. Orazem, B. Tribollet, *Electrochemical Impedance Spectroscopy*, John Wiley & Sons, Hoboken, New Jersey, **2017**.
- [44] N. Coppola, P. Polverino, G. Carapella, R. Ciancio, P. Rajak, M. Dario, F. Martinelli, L. Maritato, C. Pianese, *Materials* **2021**, *14*, 0–14.

Manuscript received: March 3, 2023
Revised manuscript received: May 6, 2023
Version of record online: June 7, 2023



Nanofibers for solid oxide fuel cells: Electrospinning is an innovative technique to obtain three-dimensional nanofiber structures. Our core-shell nanofibers employ $\text{Ce}_{0.9}\text{Gd}_{0.1}\text{O}_{1.95}$ fluorite as the core material and $\text{La}_{1-x}\text{Sr}_x\text{MnO}_3$ based perovskite as the shell.

Electrochemical impedance spectroscopy tests run on our core-shell nanofiber cathodes demonstrate a significant improvement compared to the state-of-the-art powder-based cathodes for solid oxide fuel cells.

Dr. C. Sanna, Prof. P. Costamagna*,
Dr. P. Holtappels

1 – 13

Electrochemical Impedance Spectroscopy of Core-Shell Nanofiber Cathodes, with $\text{Ce}_{0.9}\text{Gd}_{0.1}\text{O}_{1.95}$ (Core) and Cu-Doped $\text{La}_{0.6}\text{Sr}_{0.4}\text{MnO}_3$ (Shell), for Application in Solid Oxide Fuel Cells

